

# EFFECT OF STRONTIUM ADDITIONS ON THE MICROSTRUCTURAL AND MECHANICAL PROPERTIES OF Al–17Si–4Cu–0.6Mg–3Zn (B390 + 2 Wt%Zn) ALLOY

Merve Çaliş  and Ali Paşa Hekimoğlu 

Mechanical Engineering Department, Recep Tayyip Erdoğan University, Rize, Turkey

Copyright © 2022 American Foundry Society  
<https://doi.org/10.1007/s40962-022-00755-3>

## Abstract

One Al–17Si–4Cu–0.6Mg–3Zn (B390 + 2 wt%Zn) alloy and five B390 + 2 wt% Zn–Sr alloys were produced by permanent mold casting method. Microstructural evaluations were carried out with microscopic techniques. The phases of the alloys are confirmed with the X-ray diffraction (XRD) studies. The hardness, tensile strength, and elongation to fracture values of the alloys were determined by the Brinell hardness measurement method and tensile tests. It was observed that microstructure of the B390 + 2 wt%Zn alloy consisted of  $\alpha$ -Al, eutectic and primary silicon particles,  $\theta$  ( $\text{CuAl}_2$ ),  $\beta$  ( $\text{Al}_5\text{FeSi}$ ),  $\delta$  ( $\text{Al}_4\text{FeSi}_2$ ), and  $\alpha$ - $\text{Al}_{15}(\text{FeMnCu})_3\text{Si}_2$  phases. Sr addition caused significant modification in both eutectic and primary Si particles. It also caused morphology and shape changes in the other phases of the Al–17Si–4Cu–0.6Mg–

3Zn alloy. When the strontium ratio exceeded 0.075 wt%, intermetallic  $\text{Al}_2\text{Si}_2\text{Sr}$  and  $\mu$  (Al–Fe–Si–Mn) phases were formed in the alloy. Hardness and tensile strength of the B390 + 2 wt%Zn–Sr alloys increased significantly with increasing Sr ratio up to 0.075 wt%. Elongation to fracture value of B390 + 2wt%Zn alloy increased with 0.01 wt% Sr addition, but above this level, it decreased continuously with increasing Sr content. The changes caused by the Sr additions in the mechanical properties of the tested alloys were discussed in the basis of microstructural changes observed due to Sr additions.

**Keywords:** B390 alloys, microstructure, mechanical properties, Sr additions

## Introduction

According to EN 1706 standard,<sup>1</sup> aluminum (Al)-silicon (Si)-based standard Al–Si alloys are the alloys containing a maximum of ~ 20% silicon plus one or more alloying elements. These commercial alloys are successfully used in many industrial applications, especially manufacturing of components in the automotive and aerospace industries, due to their advantages such as easy and economical manufacturability, sufficient hardness and strength for many applications, high specific strength (strength/density) and corrosion resistance, low density, and thermal expansion coefficient.<sup>2–4</sup> Hardness, strength, and tribological properties of the Al–Si alloys vary depending on the silicon and other alloying elements contents.<sup>4–6</sup> While hypoeutectic Al–Si alloys, defined as containing less than 12.6% silicon, stand out by exhibiting higher strength and ductility, hypereutectic Al–Si alloys, those containing more

than 12.6% Si, exhibit higher hardness and wear resistance.<sup>7,8</sup> The lower strength values of the hypereutectic Al–Si alloys are due to the abundance of coarse and sharp-edged primary silicon particles in their microstructure and the high stress accumulation around these particles.<sup>7,8</sup> In recent years, intensive studies have been carried out on the modification and refinement of eutectic and primary silicon particles in order to decrease stress accumulation around these particles.<sup>2,6,9,10</sup> These studies showed that morphology of the eutectic silicon particles in hypoeutectic or near eutectic Al–Si alloys can be modified from acicular to fibrous by the addition of elements such as strontium (Sr) and sodium (Na) and the size of the primary Si particles can be reduced by refinement with phosphorous (P) additions, usually in the form of phosphorus-copper.<sup>11</sup> These types of modifications and refinements result in an increase in strength of Al–Si-based alloys.<sup>11–14</sup> However, there is not enough study on the modification of eutectic silicon particles in the hypereutectic Al–Si-based alloys. In addition, intensive studies are still carried out to determine the most suitable alloying element and chemical composition for the

**Table 1. Chemical Compositions of the Commercial B390 and Al-15Sr Master Alloys**

Alloy	Chemical composition (wt%)												
	Si	Cu	Mg	Zn	Sr	Fe	Mn	Cr	Ba	P	Ca	Other (Ni, Sn, Ti, etc)	Al
B390	17.68	4.38	0.62	1.21	–	1.06	0.10	0.017	–	–	–	0.14	Balance
Al-15Sr	0.036	–	< 0.05	–	14.78	0.10	–	–	0.036	< 0.01	< 0.01	< 0.21	Balance

refinement of primary silicon particles which are especially more predominant silicon phase in the microstructure of hypereutectic Al-Si alloys.<sup>15–18</sup>

Among the hypereutectic alloys, the commercialized and standardized Al-17Si-based 390 alloy is often preferred in the production of engine cylinder blocks, pumps, compressors, transmission components, and pistons due to its superior hardness and wear resistance.<sup>11</sup> However, in order to expand the usage area of the 390 alloys or to increase its

performance, quite a few studies on improving its hardness, strength, and wear properties have been conducted by researchers.<sup>3,7,11,18–23</sup> In these studies, it was revealed that mechanical and wear properties of the 390 alloys can be improved by the addition of alloying or/and modification elements and using casting method having high cooling rate. One of these studies,<sup>7</sup> revealed that the B390 (Al-17Si-4Cu-0.6Mg-1Zn) + 2 wt%Zn alloy, which is produced by permanent mold casting method and contains 2 wt%Zn more than the commercial B390 alloy, exhibits

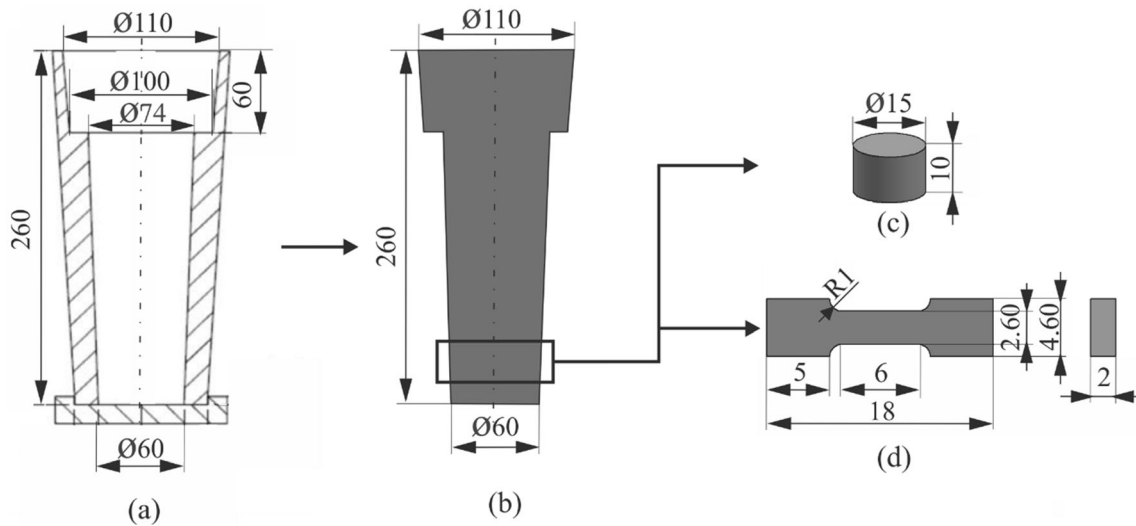


**Figure 1. Technical drawing of (a) mold, (b) alloy ingot, c metallography and hardness test sample, and (d) tensile test sample (dimensions in mm).**

**Table 2. Chemical Compositions of the Experimental Alloys**

Alloy	Chemical composition (wt%)										Al
	Si	Cu	Mg	Zn	Sr	Impurity elements					
	Fe	Mn	Cr	Other (Ni, Sn, Ti, etc)							
B390 + 2 wt%Zn	17.02	4.13	0.51	2.96	–	1.00	0.12	0.020	0.12		Balance
B390 + 2wt%Zn – 0.01Sr	17.84	4.41	0.54	2.93	0.008	1.34	0.14	0.020	0.13		Balance
B390 + 2 wt%Zn – 0.05Sr	17.99	4.41	0.55	2.94	0.040	1.30	0.14	0.020	0.25		Balance
B390 + 2 wt%Zn – 0.075Sr	17.20	4.41	0.54	2.98	0.074	1.29	0.14	0.018	0.22		Balance
B390 + 2 wt%Zn – 0.1Sr	18.14	4.13	0.52	2.80	0.100	1.27	0.14	0.012	0.20		Balance
B390 + 2 wt%Zn – 0.2Sr	18.57	4.23	0.51	2.84	0.190	1.23	0.13	0.020	0.22		Balance

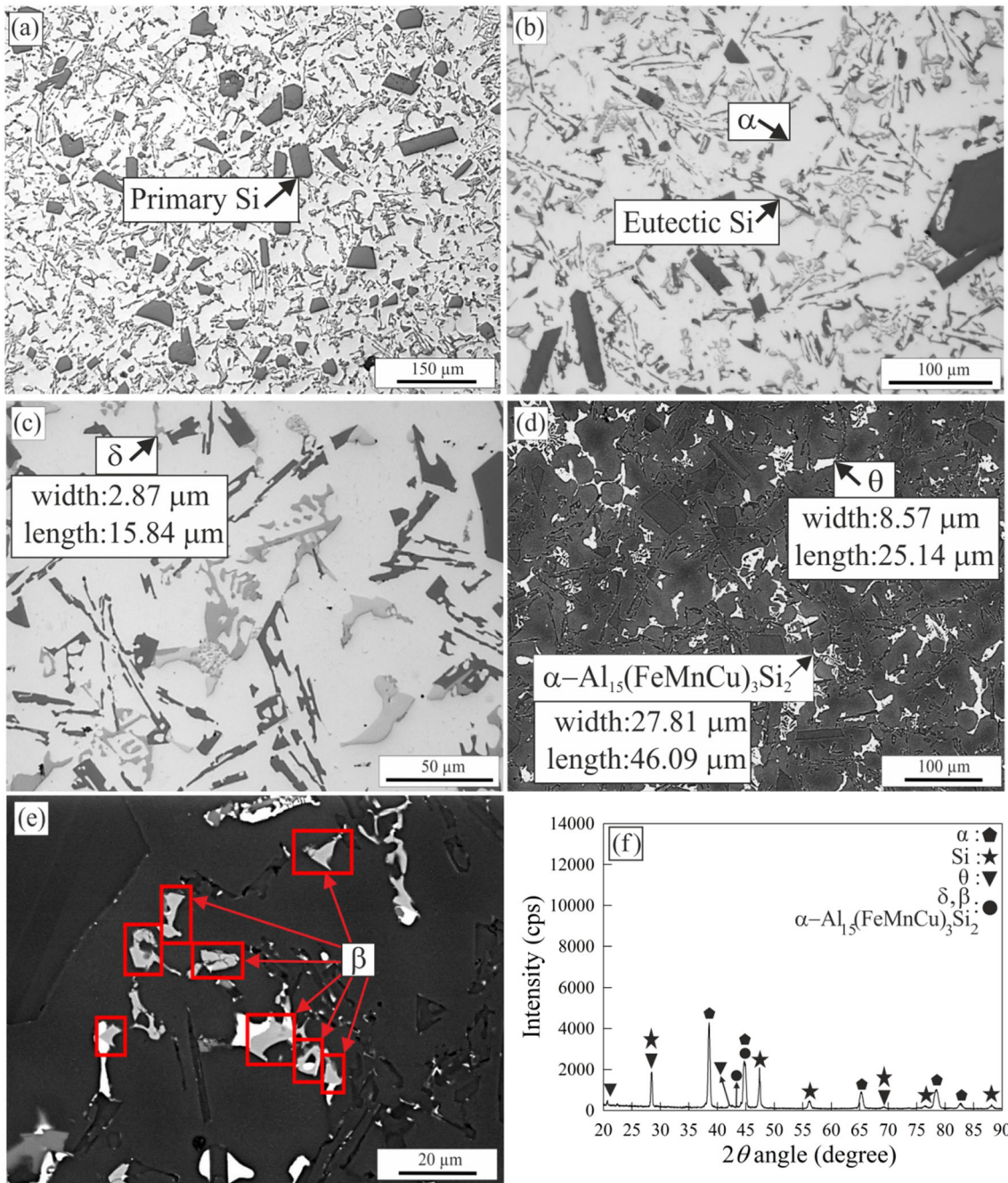


**Figure 2. (a) 100X OM, (b) 200X OM, (c) 500X OM (d) 200X SEM, and (e) 1000X SEM micrographs, and (f) XRD pattern showing the phases in the microstructure of the B390 + 2 wt%Zn alloy.**

superior hardness, strength, and wear resistance compared to the commercial B390 alloy. The strength increase in this alloy resulted with Zn addition was attributed on the solid solution strengthening mechanism, which is formed as a result of the dissolution of zinc in aluminum-rich phases. However, strengthening caused by modifying of eutectic silicon particles and refining of primary silicon particles in the B390 + 2 wt%Zn alloy which contains significant amount of eutectic and primary Si particles have not been investigated yet. Therefore, the purpose of this study is to investigate the effect of Sr which is one of the most widely

used modifier element for especially eutectic Si particles in Al-Si alloys on the microstructural and mechanical properties of the B390 + 2 wt%Zn alloy produced by permanent mold casting and to determine the optimum Sr content for this new alloy.

### Experimental Method

One B390+2 wt%Zn alloy and five B390+2 wt%Zn-Sr alloys containing different ratios of strontium up to

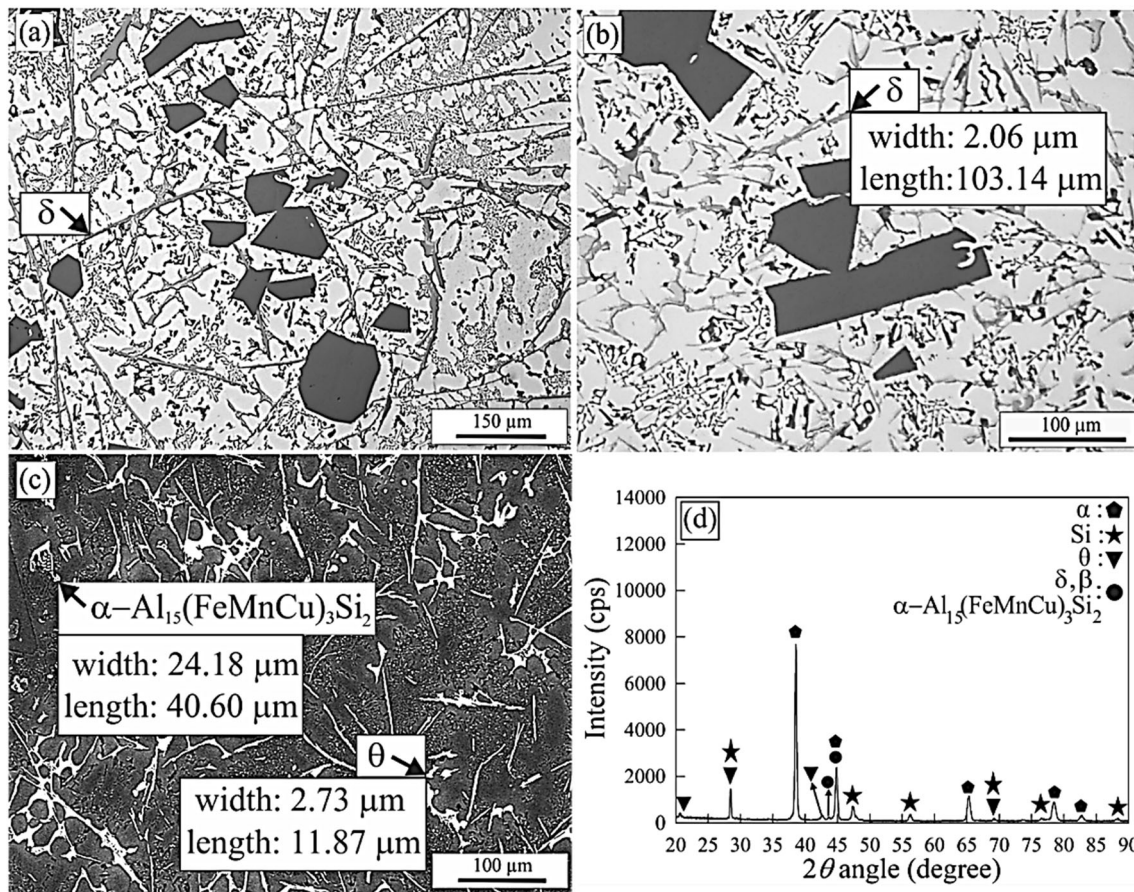


**Figure 3. (a) 100X OM, (b) 200X OM and (c) 200X SEM micrographs, and d) XRD pattern showing the phases in the microstructure of the B390 + 2 wt%Zn – 0.01Sr alloy.**

0.2 wt% were produced by induction melting method. In the production of alloys, commercial B390.1 alloy ingot, zinc with a purity degree of 99.9%, and Al–15Sr master alloy were used. Chemical compositions of the commercial B390 and Al–15Sr master alloys are given in Table 1. A mixture of 5 kg of appropriate alloying elements for each alloy was melted in a medium frequency induction furnace having a power of 50 kW and a SiC crucible to a temperature of 760 °C. The molten alloys were mixed and then poured at a casting temperature of approximately 760 °C into an uncoated SAE 8620 steel mold kept at room temperature. The technical drawing of this mold is given in Figure 1a. Chemical composition of all the experimental alloys was analyzed by spark optical emission spectrometer (Spark OES). Each alloy sample was analyzed five times and the average value of these results obtained was reported as the chemical composition of the alloy. These analysis samples were machined by the diamond cutter and Al–Si–Zn-based HYDRO-made reference material was used in these analyzes.

Microstructural evaluations were carried out using optical and electron microscopy on samples prepared by standard metallographic methods. Metallography samples were ground with 300, 600, 1200, and 2000 number SiC grinding paper and then polished with 9 and 3 μm diamond and 0.05 μm SiO<sub>2</sub> suspensions, respectively. Micrographs were taken on the polished samples without etching. The phases in the microstructures of the experimental alloys were determined by energy dispersive spectroscopy (EDS) and X-ray diffraction (XRD) analyzes. Size of the phases was calculated by a standard linear intercept method according to the ASTM E112-10 standard.<sup>24</sup> The densities of the alloys were determined by the Archimedes method. Hardness and tensile test samples were prepared by machining with water jet from the bottom of the alloy ingots whose technical drawing is given in Figure 1b. Technical drawings of these test samples are given in Figure 1c and d. The hardness of the alloys was measured with the Brinell measurement method using a 2.5 mm ballpoint under a load of 62.5 kg × f. At least six hardness measurements were performed in each alloy sample and average of the obtained values was taken as hardness value

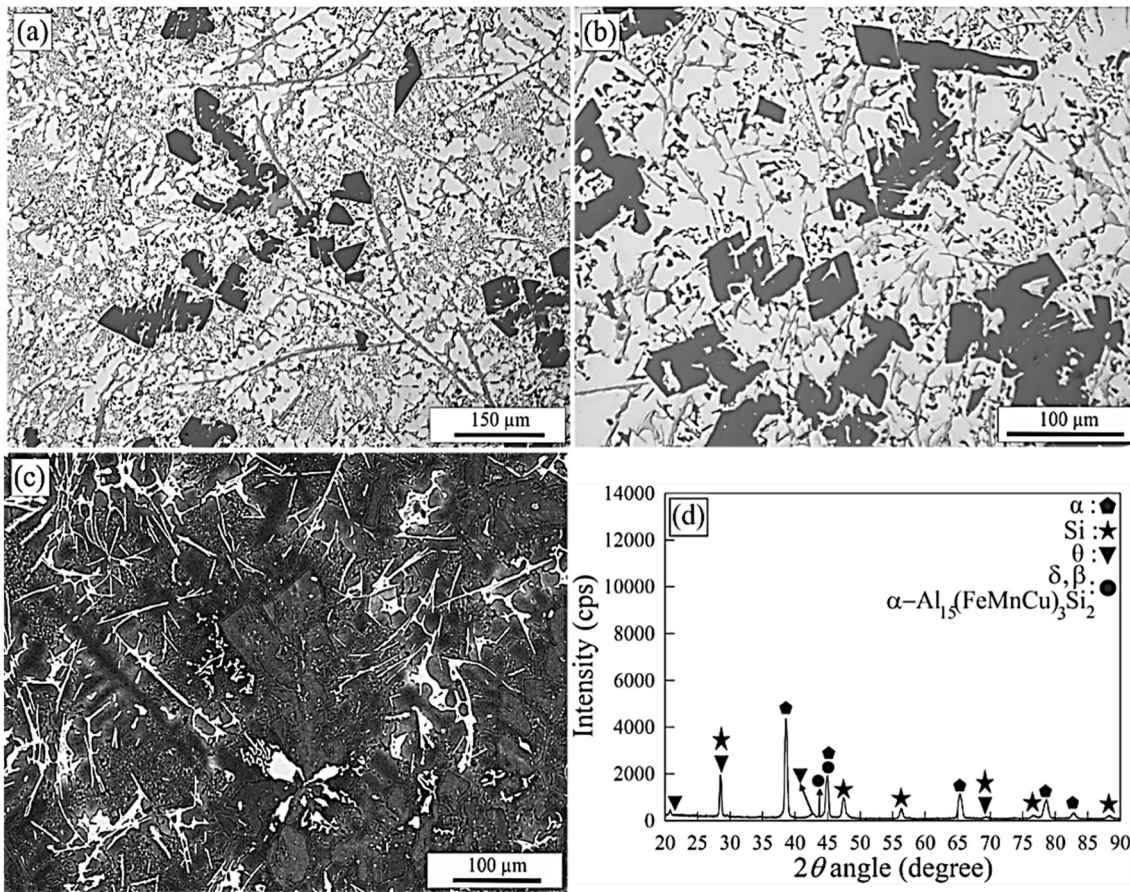


**Figure 4.** (a) 100X OM, (b) 200X OM and (c) 200X SEM micrographs, and (d) XRD pattern showing the phases in the microstructure of the B390 + 2 wt%Zn-0.05Sr alloy.

of the alloy. Tensile tests were carried out at a deformation rate of  $10^{-3} \text{ s}^{-1}$  on the samples whose technical drawing is given in Figure 1d. At least six tensile tests were carried out for each alloy. The values obtained from these tests were averaged and tensile strength and elongation to fracture values of the alloys were determined.

## Results and Discussion

### Microstructural Analysis

Chemical compositions of the experimental alloys are given in Table 2.

Micrographs and XRD patterns showing the phases in the microstructure of the B390+2 wt%Zn – (0–0.2)Sr alloys are given in Figures 2, 3, 4, 5, 6 and 7 and EDS analysis results showing the chemical compositions of phases observed in the microstructure of the experimental alloys are given in Table 3 and 4. Microstructure of the

B390 + 2 wt%Zn alloy consisted of  $\alpha$ -aluminum (Al) phase, eutectic and primary silicon particles,  $\theta$  ( $\text{CuAl}_2$ ),  $\beta$  ( $\text{Al}_5\text{FeSi}$ ),  $\delta$  ( $\text{Al}_4\text{FeSi}_2$ ), and  $\alpha\text{-Al}_{15}(\text{FeMnCu})_3\text{Si}_2$  phases, Figure 2. Eutectic silicon particles have acicular morphology while primary silicon particles have an irregularly blocky shaped coarse structure with sharp edges and corners. These silicon particles show a random distribution in the microstructure, Figure 2. The copper-rich  $\theta$  phase is formed among the  $\alpha$  regions, and the  $\alpha\text{-Al}_{15}(\text{FeMnCu})_3\text{Si}_2$  phase is formed within the  $\alpha$ -aluminum phase regions or on the intermetallic  $\theta$  phase, Figure 2. The formation of  $\alpha$ -aluminum phase, silicon particles, and  $\theta$  ( $\text{CuAl}_2$ ) phase has been explained in detail in the literature.<sup>7</sup> The  $\delta$  ( $\text{Al}_4\text{FeSi}_2$ ),  $\beta$  ( $\text{Al}_5\text{FeSi}$ ), and  $\alpha\text{-Al}_{15}(\text{FeMnCu})_3\text{Si}_2$  phases observed in the microstructure of the test alloys are intermetallic compounds formed in Al-Si alloys as a result of the reaction of impurity elements with alloying elements during casting.<sup>25,26</sup> Therefore, the formation of these phases is thought to vary depending on the impurity elements in the chemical composition of the alloy and the ratio of these elements. Relevant studies in the literature exhibit that

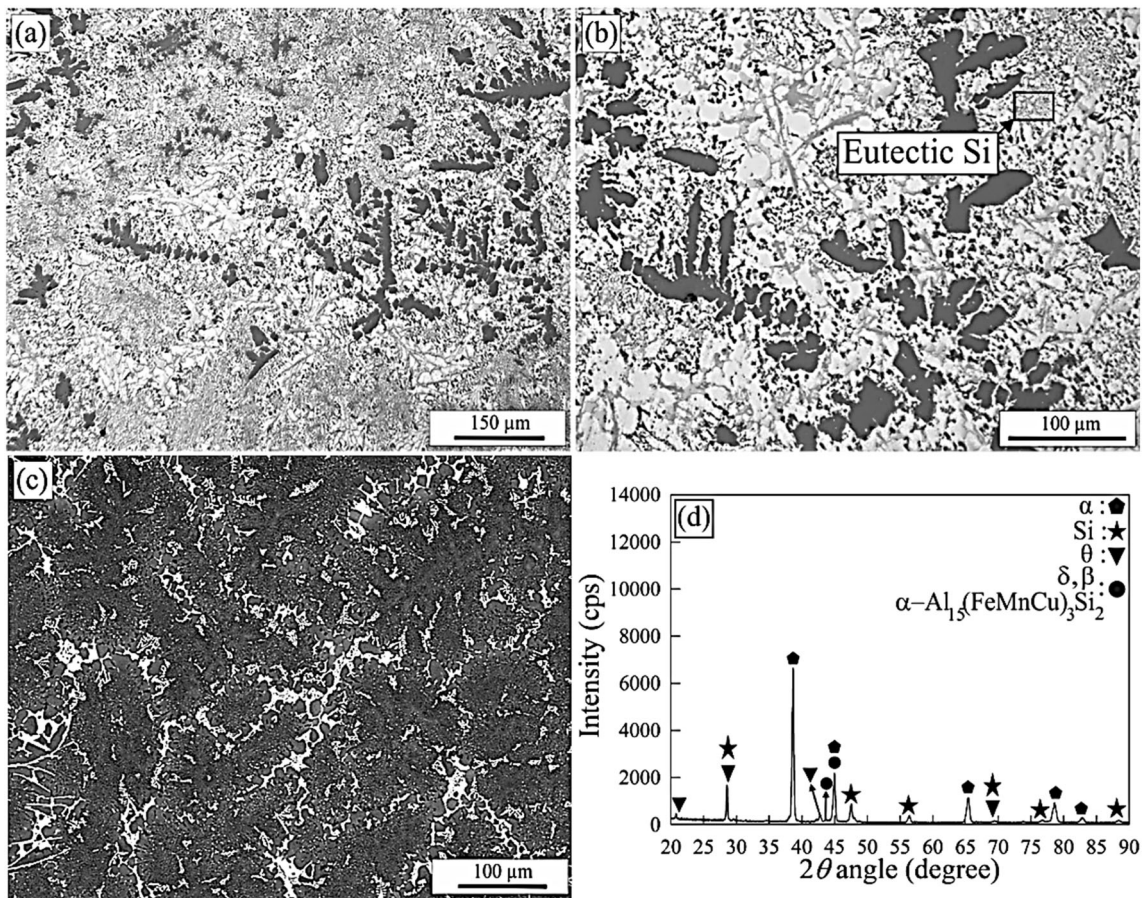


**Figure 5. (a) 100X OM, (b) 200X OM and (c) 200X SEM micrographs, and (d) XRD pattern showing the phases in the microstructure of the B390 + 2 wt%Zn – 0.075Sr alloy.**

different intermetallic phases are formed in Al-Si alloys containing different ratios of impurity elements especially iron.<sup>26–29</sup> It is suggested that iron-rich intermetallic phases in Al-Si alloys will be formed when the sludge factor (Eqn. 1) is higher than 1.25, and the ratio of these intermetallic phases will increase as the Fe/Mn ratio increases.<sup>28,30,31</sup> In addition, it is found out that if the Fe/Mn ratio is greater than 2, Mn and Cr elements in the  $\beta$  phase will react with iron to form the  $\alpha\text{-Al}_{15}(\text{FeMnCu})_3\text{Si}_2$  phase.<sup>28,30,31</sup> The sludge factor values and Fe/Mn ratios calculated for the experimental alloys given in Table 5 show that the results we obtained are compatible with this literature information.

$$\text{Sludge factor (SF)} = (1 \times \% \text{ Fe}) + (2 \times \% \text{ Mn}) + (3 \times \% \text{ Cr})$$

Eqn. 1

The intermetallic  $\delta$  ( $\text{Al}_4\text{FeSi}_2$ ) phase is formed with reaction of liquid iron which is an impurity element with aluminum and silicon.<sup>29</sup> This phase transforms into the  $\beta$  ( $\text{Al}_5\text{FeSi}$ ) phase with the peritectic reaction ( $\text{Liquid} + \delta - \text{Al}_4\text{FeSi}_2 \rightarrow \beta - \text{Al}_5\text{FeSi} + \text{Si}$ )<sup>27</sup> during cooling. It is plausible to say that the transformation of phase  $\delta$  with a relatively high silicon ratio into  $\beta$  phase having lower silicon ratio occurs by diffusion mechanism.

The coexistence of  $\delta$  and  $\beta$  phases in the microstructure of the alloys may be due to the inability of this transformation to be fully realized because of factors such as non-equilibrium cooling conditions, short solidification or diffusion time, and high silicon content in the alloy. It is known that the intermetallic  $\alpha\text{-Al}_{15}(\text{FeMnCu})_3\text{Si}$  phase is formed as a result of the reaction of the  $\beta$  phase with an impurity element Mn ( $\text{Liquid} + \beta\text{-Al}_{15}\text{FeSi} \rightarrow \text{Al} + \text{Si} + \alpha\text{-Al}_{15}(\text{FeMnCu})_3\text{Si}_2$ ).<sup>26–28,31</sup>

It was observed that Sr addition caused morphology changes in all the phases of the B390+2wt%Zn alloy, but these changes were more pronounced in eutectic and primary silicon particles, Figures 3, 4, 5, 6 and 7. Addition of 0.075 wt% Sr to the B390 + 2 wt%Zn alloy led to a significant reduction in the size and aspect ratio of the primary silicon particles, but Sr additions higher than this ratio did not significantly affect the size of these particles while causing an increase in aspect ratio, Figures 8 and 9. After Sr additions are increased, the morphologies of eutectic Si and primary Si were observed to change from acicular to fibrous form and blocky to flower-like form, respectively. These changes caused by the addition of strontium are explained in the literature<sup>29,33</sup> based on the change in solidification conditions after casting. It is known that the

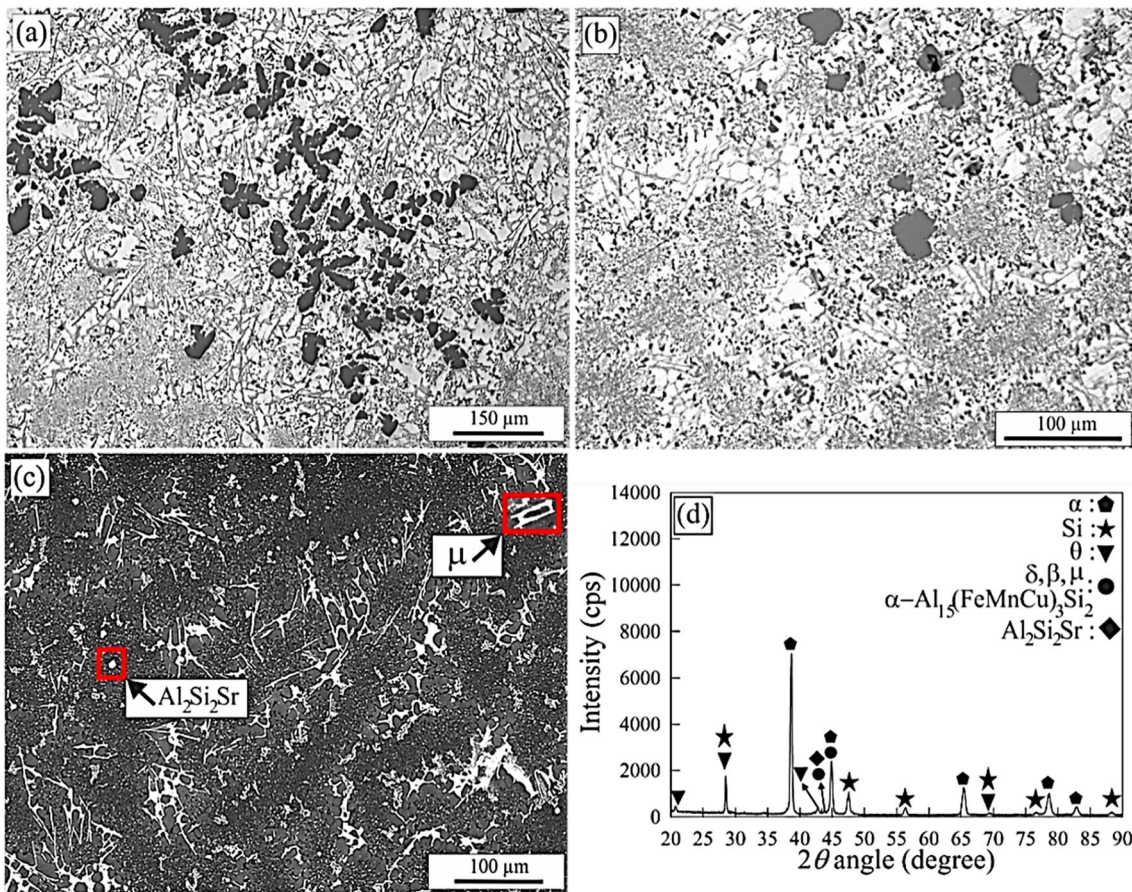


**Figure 6. (a) 100X OM, (b) 200X OM and (c) 200X SEM micrographs, and (d) XRD pattern showing the phases in the microstructure of the B390 + 2 wt%Zn – 0.1Sr alloy.**

addition of strontium causes an increase in the heat released during eutectic transformation, and a decrease in the eutectic transformation temperature compared to Al-Si alloys which have not contain strontium, a shift of the eutectic point to the higher silicon ratio.<sup>34–37</sup> This results in the start of nucleation at a lower temperature. The decrease in the nucleation temperature prevents the solidification around the eutectic silicon nuclei. This makes difficult nuclei growth and causes eutectic silicon particles to remain small. It was observed that the addition of Sr caused a change in morphology of the primary Si particles in the microstructure of the B390+2wt%Zn alloy (Figures 3 and 4) and these particles exhibited a flower-like or dendritic morphology if the alloy contained 0.075wt% Sr, Figure 5. The change in the morphology of the primary Si particles due to Sr addition is explained by the preventing of the twin plane edge addition (Twin Plane Reentrant Edge (TPRE)) mechanism that ensures the growth of primary silicon particles.<sup>38,39</sup> The dstructure or morphology of primary silicon particles depends on their nucleation and growth behavior,<sup>40</sup> and these particles tend to directional growth and are anisotropic. However, with the addition of strontium the TPRE mechanism is negatively affected, prevents the growth of primary silicon particles in separate

directions, and the silicon particles remain smaller. It is known that local prevention of the growth of silicon particles leads to the formation of dendritic structure.<sup>38–40</sup> It was observed that if the strontium ratio exceeded 0.075 wt%, the dendritic structure of the silicon phase was broken down and the primary silicon particles regrew with the increasing Sr ratio, Figures 6 and 7. It is stated in the literature that this is due to the decrease in the grain growth temperature when the strontium ratio in Al-Si alloys exceeds certain values, and the decrease in the nucleating effect due to the formation of the  $\text{Al}_2\text{Si}_2\text{Sr}$  intermetallic phase.<sup>41</sup>

Figures 2 and 3 show that the  $\theta$ ,  $\delta$ , and  $\alpha\text{-Al}_{15}(\text{FeMnCu})_3\text{Si}_2$  phases become slightly thinner with the addition of strontium to the Al–17Si–4Cu–0.6Mg–3Zn alloy. It was observed that when 0.01 wt% Sr was added to the B390 + 2 wt%Zn alloy, the iron-containing  $\delta$  phase grew in a thin elongated form, but this phase shrank up to 0.075 wt%Sr with increasing Sr ratio, and after this ratio, it started to grow again, Figures 3, 4, 5, 6 and 7. It was also observed that when the strontium ratio exceeded 0.075 wt%, intermetallic  $\text{Al}_2\text{Si}_2\text{Sr}$ , and  $\mu$  (Al–Fe–Si–Mn) phases were formed in the microstructure of

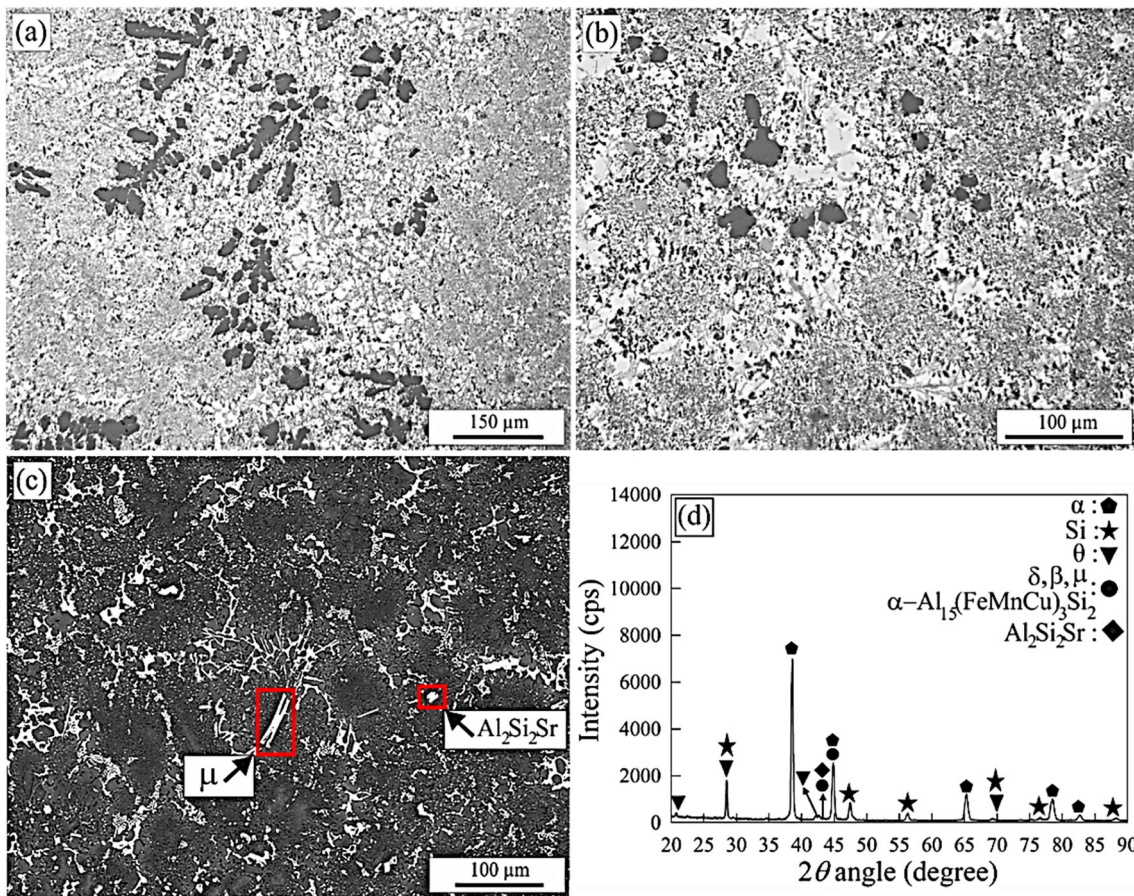


**Figure 7. (a) 100X OM, (b) 200X OM and (c) 200X SEM micrographs, and (d) XRD pattern showing the phases in the microstructure of the B390+2 wt%Zn – 0.2Sr alloy.**

B390 + 2 wt%Zn–Sr alloys, Figures 6 and 7. The literature reveals that the  $\text{Al}_2\text{Si}_2\text{Sr}$  intermetallic phase is formed as a result of the decrease in the nucleation temperature of the silicon due to the increase in the cooling rate with the addition of strontium and the effect of poisoning on the nucleation zones<sup>41,42</sup> The intermetallic  $\mu$  phase having high iron content is thought to be an unstable phase that has not transformed due to its high cooling rate.

$2\theta$  (Bragg) angles of the phases in the microstructure of the alloys studied are determined as  $38^\circ$ ,  $45^\circ$ ,  $65^\circ$ ,  $78^\circ$ , and  $83^\circ$  for the  $\alpha$ -Al phase,  $28^\circ$ ,  $47^\circ$ ,  $56^\circ$ ,  $69^\circ$ ,  $76^\circ$ , and  $88^\circ$  for the silicon,  $28^\circ$ ,  $45^\circ$ ,  $56^\circ$ , and  $69^\circ$  for  $\theta$ , and  $44^\circ$  and  $45^\circ$  for the iron-rich intermetallic  $\beta$ ,  $\delta$ ,  $\alpha\text{-Al}_{15}(\text{FeMnCu})_3\text{Si}_2$ , and  $\mu$  phases, Figures 2f, 3d, 4d, 5d, 6d, and 7d. In addition, it has been observed that when the strontium ratio reaches 0.1 wt% in B390 + 2 wt%Zn–Sr alloys, the  $\text{Al}_2\text{Si}_2\text{Sr}$  phase peak is formed at  $44^\circ$  and  $69^\circ$ , Figures 6d. The absence of these peaks in the alloys having Sr less than 0.1% may have been caused by the solution of strontium in the phases constituting the alloys.

## Physical and Mechanical Tests

Density, hardness, tensile strength, and elongation to fracture values of the tested alloys are given in Table 6, and the curves showing the variation of these values with the strontium ratio are given in Figure 10. Density of the tested alloy did not show significant change with Sr additions, Table 6 and Figure 10. It was observed that the hardness of B390 + 2 wt% Zn + Sr alloys increased up to 0.075wt% Sr content and decreased after this ratio and reached constant values, Figure 10. The increase in hardness may have resulted from reduction of the size and increase in number of the Si particles in the microstructure of the alloy (Figure 9), and therefore dispersion hardening mechanism becoming more effective. Decrease observed in hardness of the alloys after 0.075 wt% Sr ratio may be due to decrease in the primary silicon ratio in the microstructure because of the shift of the eutectic point to a higher silicon ratio. In addition, the decrement of the solid solution hardening effect due to growth of the  $\delta$  phase and the formation of  $\mu$  and  $\text{Al}_2\text{Si}_2\text{Sr}$  phases may have contributed to the decrease in hardness. It was observed that the tensile strength of B390+2 wt% Zn+Sr alloys increased up to 0.075 wt% Sr content, then decreased, Figure 10. It was also observed



**Table 3. Chemical Compositions of the  $\alpha$ , Eutectic Al, and  $\theta$  Phases**

Alloy	Chemical composition (wt%)											
	$\alpha$ phase			Eutectic Al phase			$\theta$ phase					
	Al	Zn	Cu	Si	Al	Zn	Cu	Si	Al	Cu	Si	Zn
B390 + 2 wt%Zn	88.1–94.5	0.6–2.9	2.1–3.9	2.9–18.6	57.7–91.1	1.7–2.9	2.6–2.9	2.3–7.3	47.6–61.7	29.1–49.1	0.6–1.8	1.5–1.7
B390 + 2wt%Zn – 0.01Sr	79.3–92.9	2.2–4.7	1.3–3.6	1.5–17.2	49.9–83.4	1.9–3.0	1.0–2.9	2.9–10.8	48.2–51.2	45.8–48.8	0.8–1.1	1.7–2.3
B390 + 2 wt%Zn – 0.05Sr	82.5–91.2	2.4–2.9	1.3–2.1	1.0–13.1	65.4–89.9	1.8–3.0	1.2–3.0	5.3–30.9	48.7–62.6	31.2–45.8	0.9–2.1	1.7–2.4
B390 + 2 wt%Zn – 0.075Sr	66.9–91.1	1.6–5.7	1.1–2.7	1.4–19.5	72.9–86.8	1.6–3.0	0.6–3.0	9.7–25.0	44.3–58.4	29.9–48.5	1.0–1.4	1.8–2.2
B390 + 2 wt%Zn – 0.1Sr	70.1–94.3	3.5–4.9	2.2–3.4	1.5–17.2	79.1–83.3	1.4–2.8	1.4–3.0	3.1–16.7	50.0–61.8	35.7–48.3	0.7–1.5	1.3–2.3
B390 + 2 wt%Zn – 0.2Sr	70.5–93.5	3.7–4.1	1.9–3.7	1.5–13.9	72.1–89.3	1.7–3.0	1.8–2.8	7.4–17.9	45.7–52.9	30.0–54.0	0.8–2.0	1.5–2.4

that the elongation to fracture value of the B390+2 wt%Zn alloy increases with 0.01 wt%Sr addition, but it decreases with increasing Sr additions, Figure 10. The increase in tensile strength with the addition of Sr is thought to be mainly due to modification of eutectic silicon particles, shape and/or morphology change and size reduction in the primary silicon particles. With increasing Sr contents, morphology of the primary silicon particles changed from sharp-edged coarse blocky form to flower-like or dendritic form and eutectic silicon particles changed from acicular form to fibrous form. In addition, number of the eutectic and primary Si particles increased due to modification, and these particles exhibited a more homogenous dispersion. These microstructural changes are thought to be the main reason for the increase in the strength of the alloy. It is well known that the increase in strength is associated with the number of particles preventing the movement of dislocations and more homogeneous distribution of particles.<sup>43–47</sup> Effect of more homogeneous and closer arrangement of particles in the microstructure on the strength is expressed by the (Eqn. 2),<sup>48</sup> where  $\tau_a$  is the stress value required for dislocation to overcome obstacles (and to form new ones),  $G$  is the shear modulus,  $b$  is the Burgers vector and  $L$  is the distance between particles. As it can be understood from this equation, when the distance between particles decreases, the  $\tau_a$  value and therefore the material strength increases. In addition to the modification in the silicon particles, shrinkage which was observed in the  $\delta$  and  $\alpha$ -Al<sub>15</sub>(FeMnCu)<sub>3</sub>Si<sub>2</sub> phases up to 0.075 wt%Sr content may have also contributed to the increase in tensile strength. When the Sr ratio in the experimental alloys exceeds 0.075%, the decrease in the tensile strength of the tested alloys may be due to the increase in aspect ratio, breakdown of the dendritic structure of the primary silicon phase, and the effect of the stress concentrations which may occur around the Al<sub>2</sub>Si<sub>2</sub>Sr and  $\mu$  (Al, Fe, Si) phases forming after 0.1 wt% Sr content. The increase in elongation to fracture with the addition of Sr may have been caused by morphology changes in the phases, especially silicon particles. The decrease in elongation to fracture values with increasing Sr ratio is thought to be caused by the decrease in the volumetric ratio of the ductile  $\alpha$ -Al phase in the structure, the increase in ratio of the relatively hard eutectic phase, and the formation of intermetallic Al<sub>2</sub>Si<sub>2</sub>Sr and  $\mu$  (Al, Fe, Si) phases. It is known from the literature that intermetallic phases formed in the microstructure of the alloys facilitate the fracture and thus reduce the values of elongation to fracture.<sup>2,14,44,45,49,50</sup>

$$\tau_a = 2Gb/L \tag{Eqn. 2}$$

It was observed that the fracture surfaces of the alloys were generally formed from cleavage planes formed by the fracture of the silicon particles, rupture ridges caused by aluminum-rich phases and partially cracks, Figure 11. Cleavage planes are accepted as brittle fracture and rupture ridges are accepted as ductile fracture.<sup>51,52</sup> No significant

**Table 4. Chemical Composition of the Intermetallic Phases**

Phase	Chemical composition (wt%)							
	Al	Si	Fe	Sr	Zn	Mn	Cu	Cr
$\beta$	57.7–66.5	7.2–10.5	16.2–21.9	–	–	–	–	–
$\delta$	49.7–69.7	13.7–25.7	13.9–21.5	–	1.2–2.1	1.5–2.0	1.4–3.0	–
$\alpha$ - $\text{Al}_{15}(\text{FeMnCu})_3\text{Si}_2$	51.8–80.1	5.3–11.3	5.6–23.1	–	1.2–4.4	0.7–2.9	3.3–7.7	0.5–0.8
$\mu$	40.7–41.5	30.4–31.0	23.9–25.0	–	–	2.9–3.1	–	–
$\text{Al}_2\text{Si}_2\text{Sr}$	28.4–31.3	26.0–30.1	–	39.0–40.1	–	–	–	–

**Table 5. Sludge Factors of the Alloys**

Alloy	Fe	Mn	Cr	Sludge factor	Fe/Mn ratio
B390 + 2 wt%Zn	1.00	0.12	0.020	1.30	8.33
B390 + 2wt%Zn – 0.01Sr	1.34	0.14	0.020	1.68	9.57
B390 + 2 wt%Zn – 0.05Sr	1.30	0.14	0.020	1.64	9.28
B390 + 2 wt%Zn – 0.075Sr	1.29	0.14	0.018	1.62	9.21
B390 + 2 wt%Zn – 0.1Sr	1.27	0.14	0.012	1.58	9.07
B390 + 2 wt%Zn – 0.2Sr	1.23	0.13	0.020	1.57	9.46

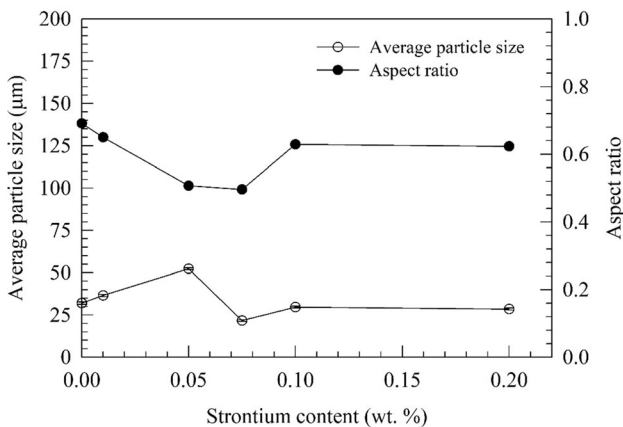


**Figure 8. The curves showing the variation of size and aspect ratio values of primary silicon particles in B390 + 2 wt%Zn–Sr alloy with strontium ratio.**

change was observed in the fracture surfaces of the B390 + 2% Zn alloy due to Sr additions, Figure 11. SEM micrographs showing longitudinal sections below fracture surfaces of tensile test sample of the experimental alloys are given in Figure 12. These photographs show that the cracks cannot propagate through  $\alpha$ -Al dendrites and they progress by entangling their boundaries, but if intermetallic phases such as  $\theta$ ,  $\beta$ ,  $\delta$ , and  $\alpha$ - $\text{Al}_{15}(\text{FeMnCu})_3\text{Si}_2$  are present at the boundaries of the

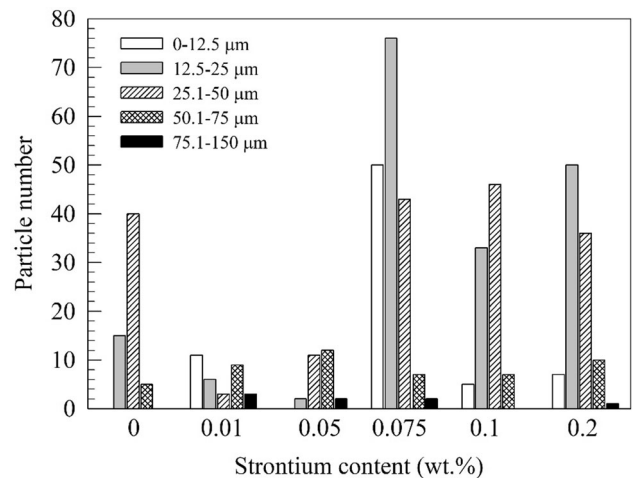


**Figure 9. The bar chart diagram showing the distribution of number and size of primary silicon particles in B390 + 2 wt%Zn – (0 – 0.2)Sr alloys.**

dendrites, the fracture proceeds through these intermetallic phases. It is thought that the preferential progression of the fracture line over intermetallic phases is due to the fact that these phases are more brittle than the  $\alpha$ -Al phase as it is also pointed in the relevant literature.<sup>50-53</sup>

**Table 6. Density, Hardness, Tensile Strength, and Elongation to Fracture Values of the Alloys (Standard Deviation Values were Calculated for Confidence Level of 96%).**

Alloy	Density (gr/cm <sup>3</sup> )	Hardness (HBN)	Standard deviation	Tensile strength (MPa)	Standard deviation	Elongation to fracture (%)	Standard deviation
B390 + 2 wt%Zn	2.76	113±1.5	1.23	161±6.2	5.06	3.4±1.6	1.31
B390 + 2wt%Zn – 0.01Sr	2.77	115±1.2	0.98	165±5.6	4.57	3.5±1.2	0.98
B390 + 2 wt%Zn – 0.05Sr	2.77	119±1.1	0.90	172±7.3	5.96	3.4±1.8	1.47
B390 + 2 wt%Zn – 0.075Sr	2.78	122±1.3	1.06	189±6.4	5.23	2.6±1.5	1.23
B390 + 2 wt%Zn – 0.1Sr	2.77	115±1.0	0.82	151±8.1	6.61	2.4±1.2	0.98
B390 + 2 wt%Zn – 0.2Sr	2.78	115±1.3	1.06	151±7.9	6.45	2.4±1.3	1.01

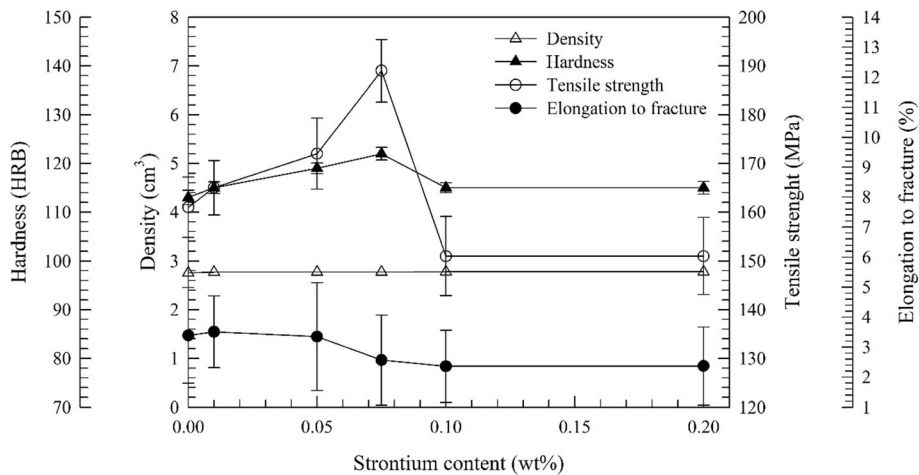


**Figure 10. Variations in hardness, density, tensile strength, and elongation to fracture of B390 + 2 wt%Zn–Sr alloys with strontium content.**

## Conclusions

In this study, effect of strontium on the microstructural and mechanical properties of B390 + 2 wt%Zn alloy has been investigated experimentally. The conclusions drawn from this study are listed below.

- Microstructure of the B390 + 2 wt%Zn alloy consists of  $\alpha$ -aluminum (Al) phase, eutectic and primary silicon particles,  $\theta$  (CuAl<sub>2</sub>),  $\beta$  (Al<sub>5</sub>FeSi),  $\delta$  (Al<sub>4</sub>FeSi<sub>2</sub>), and  $\alpha$ -Al<sub>15</sub>(FeMnCu)<sub>3</sub>Si<sub>2</sub> phases.
- Intermetallic Al<sub>2</sub>Si<sub>2</sub>Sr and  $\mu$  (Al–Fe–Si–Mn) phases are formed in the microstructure of B390 + 2 wt%Zn–Sr alloys when the strontium ratio exceeds 0.075 wt%.
- Addition of Sr causes significant modification of the eutectic silicon particles from acicular to fibrous form in the hypereutectic B390 + 2 wt%Zn alloy. Addition of Sr also

causes significant change in the size, shape, and/or morphology of the primary silicon particles,  $\theta$  (CuAl<sub>2</sub>),  $\beta$  (Al<sub>5</sub>FeSi),  $\delta$  (Al<sub>4</sub>FeSi<sub>2</sub>), and  $\alpha$ -Al<sub>15</sub>(FeMnCu)<sub>3</sub>Si<sub>2</sub> phases in the microstructure of the B390 + 2 wt%Zn alloy. However, the most obvious changes occur in primary silicon particles among these phases.

- Hardness and tensile strength of the B390 + 2 wt%Zn–Sr alloys increases up to 0.075 wt% Sr content. Elongation to fracture of the B390 + 2 wt% Zn alloy increases with 0.01 wt%Sr addition, but it decreases with increasing Sr additions.
- Fracture surfaces of the B390 + 2 wt%Zn–Sr alloys are generally formed from cleavage planes formed by the fracture of the silicon particles, rupture ridges caused by aluminum-rich phases, and partially cracks.

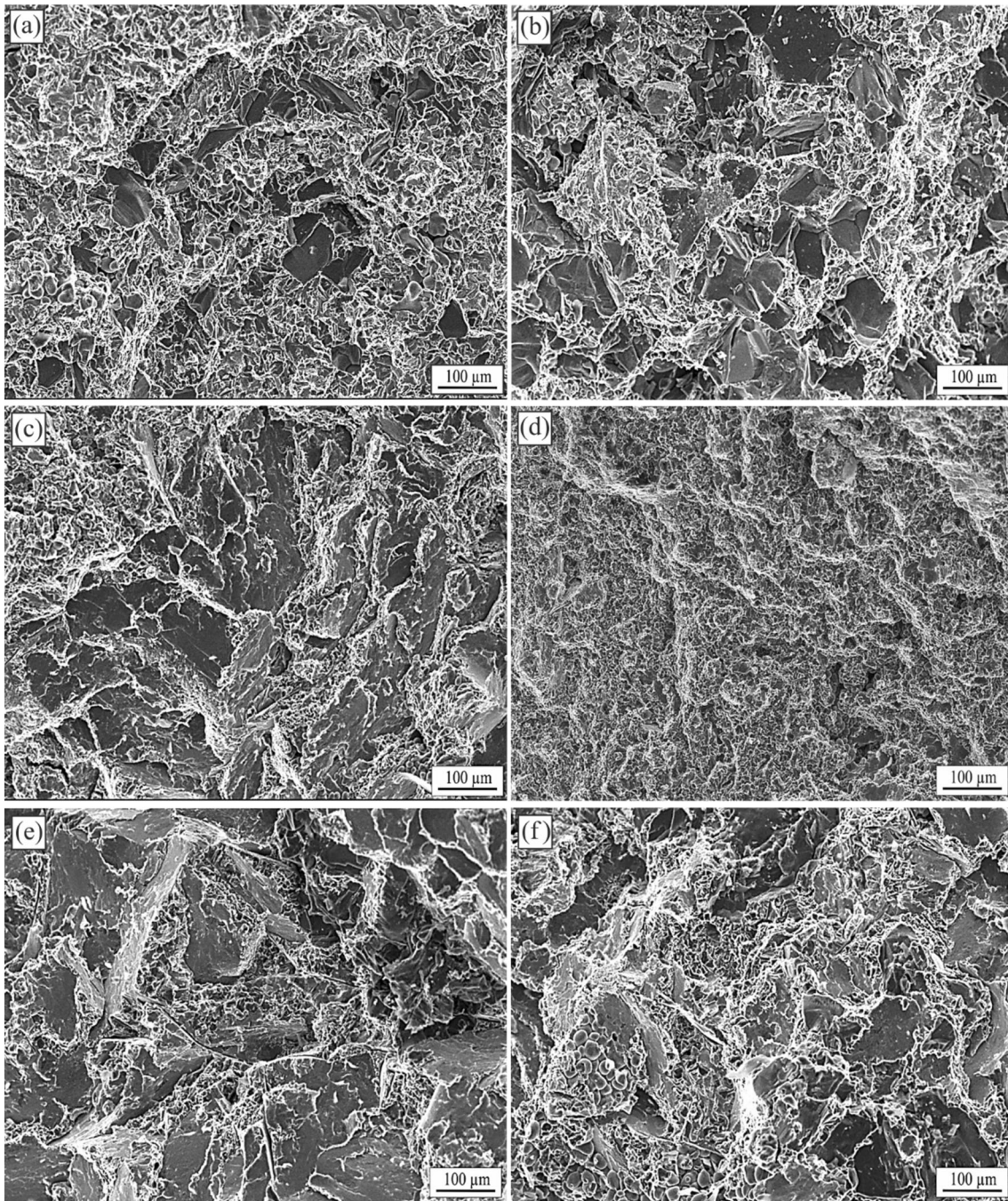


**Figure 11. Micrographs showing fracture surfaces of tensile test sample of the (a) B390 + 2 wt%Zn, (b) B390 + 2 wt%Zn - 0.01Sr, (c) B390 + 2 wt%Zn - 0.05Sr, (d) B390 + 2 wt%Zn - 0.075Sr, (e) B390 + 2 wt%Zn - 0.1Sr, and (f) B390 + 2 wt%Zn - 0.2Sr alloy.**

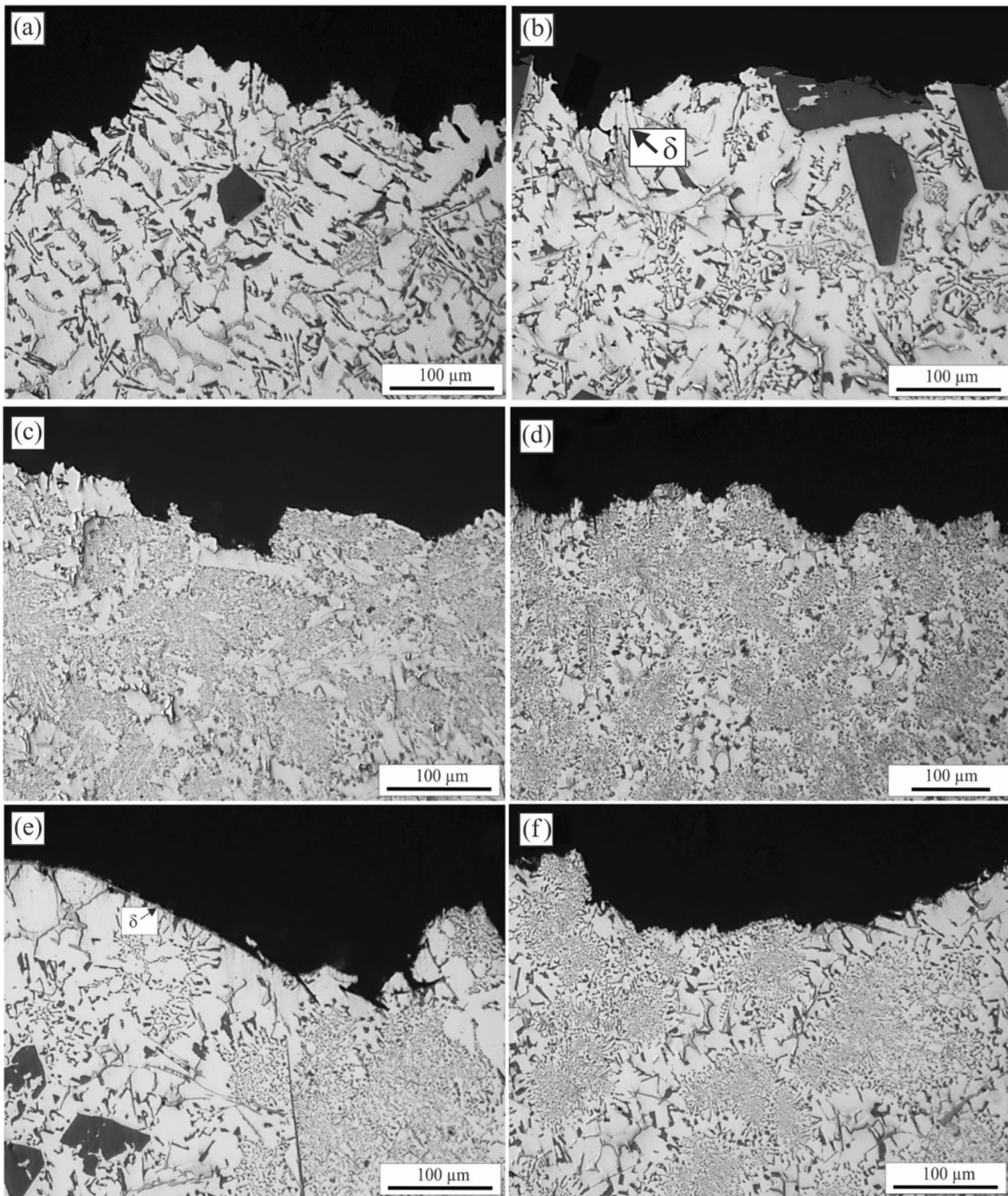


**Figure 12.** SEM micrographs showing longitudinal sections below fracture surfaces of tensile test sample of (a) B390 + 2 wt%Zn, (b) B390 + 2 wt%Zn - 0.01Sr, (c) B390 + 2 wt%Zn - 0.05Sr, (d) B390 + 2 wt%Zn - 0.075Sr, (e) B390 + 2 wt%Zn - 0.1Sr, and (f) B390 + 2 wt%Zn - 0.2Sr alloy.

### Funding

The authors did not receive support from any organization for the submitted work.

### Declarations

**Conflict of interest** The authors declare that they have no conflict of interest.

**Ethical Approval** Not applicable.

### REFERENCES

1. EN 1706:2020—Aluminium and aluminium alloys—castings—chemical composition and mechanical properties.

2. J. Scepanovic, V. Asanovic, S. Herenda et al., *Inter Metalcast.* **13**, 700–714 (2019). <https://doi.org/10.1007/s40962-019-00315-2>
3. W. Kasprzak, M. Sahoo, J. Sokolowski et al., *Inter Metalcast.* **3**, 55–71 (2009). <https://doi.org/10.1007/BF03355453>
4. M. Shamsuzzoha, L. Nastac, J. Berry, *Inter Metalcast.* **6**, 27–34 (2012). <https://doi.org/10.1007/BF03355531>
5. S.K. Shaha, F. Czerwinski, W. Kasprzak, J. Friedman, D.L. Chen, *Mater. Sci. Eng. A.* **636**, 361–372 (2015). <https://doi.org/10.1016/j.msea.2015.03.077>
6. A.P. Hekimoğlu, M. Çaliş, G. Ayata, *Met. Mater. Int.* **25**, 1488–1499 (2019). <https://doi.org/10.1007/s12540-019-00429-6>
7. A.P. Hekimoğlu, M. Haciosmanoğlu, M. Baki, *J. Fac. Eng. Archit. Gaz.* **35** (4), 1799–1814 (2020). <https://doi.org/10.17341/gazimmfd.602161>
8. A.P. Hekimoğlu, M. Haciosmanoğlu, *Microstructure and mechanical properties of Al-(2-30)Si alloys*. In: *Proceedings of 3rd International Conference on Material Science and Technology in Cappadocia (IMSTEC'18)*, pp. 169–74 (2018).
9. A.P. Hekimoğlu, M. Haciosmanoğlu, *IJERAD.* **11**(2), 685–694 (2019). <https://doi.org/10.29137/umagd.546562>
10. K.S. Zuo, H.T. Zhang, X. Han, H.L. Jia, K. Qin, J.Z. Cui, *Int. J. Met.* **8**, 55–62 (2014). <https://doi.org/10.1007/BF03355595>
11. J. Jorstad, D. Apelian, *Inter Metalcast.* **3**, 13–36 (2009). <https://doi.org/10.1007/BF03355450>
12. Q. Li, B. Li, J. Liu, J. Li, D. Liu, Y. Lan, T. Xia, *Inter Metalcast.* **13**, 367–383 (2019). <https://doi.org/10.1007/s40962-018-0242-3>
13. M. Tebib, A.M. Samuel, F. Ajersch, X.-G. Chen, *Mater. Charact.* **89**, 112–123 (2014). <https://doi.org/10.1016/j.matchar.2014.01.005>
14. Q. Li, Y. Zhu, B. Li et al., *Inter Metalcast.* **14**, 409–422 (2020). <https://doi.org/10.1007/s40962-019-00360-x>
15. R.J. Donahue, *Hypereutectic Al–Si–Mg–Sr alloy with a unique microstructure and improved ductility*. *NADCA Trans.* **T16–013**, 1–19 (2016)
16. H. Tahiri, A.M. Samuel, H.W. Doty et al., *Inter Metalcast.* **12**, 307–320 (2018). <https://doi.org/10.1007/s40962-017-0164-5>
17. K.S. Zuo, H.T. Zhang, X. Han et al., *Inter Metalcast.* **8**, 55–62 (2014). <https://doi.org/10.1007/BF03355595>
18. O. Uzun, M.F. Kılıçaslan, F. Yılmaz, *Mater. Sci. Eng. A.* **607**, 368–375 (2014). <https://doi.org/10.1016/j.msea.2014.04.025>
19. M. Schöbel, G. Baumgartner, S. Gerth, J. Bernardi, M. Hofmann, *Acta. Mater.* **81**, 401–408 (2014)
20. M.M. Shehata, S. El-Hadad, M.E. Moussa, *Inter Metalcast.* **15**, 488–499 (2021). <https://doi.org/10.1007/s40962-020-00465-8>
21. J. Hao, H. Luo, J. Bian et al., *Inter Metalcast* (2021). <https://doi.org/10.1007/s40962-021-00575-x>
22. J.W. Park, H.J. Kim, *Inter Metalcast.* **11**, 802–811 (2017). <https://doi.org/10.1007/s40962-016-0127-2>
23. S.A. Hassasi, M. Abbasi, S.J. Hosseinipour, *Inter Metalcast.* (2020). <https://doi.org/10.1007/s40962-020-00507-1>
24. ASTM E112-10 Standard test methods for determining average grain size. West Conshohocken, PA: ASTM International, 2010.
25. K. He, F. Yu, D. Zhao, L. Zuo, *Trans. Indian Inst. Met.* **62**, 367–371 (2010)
26. S. Kores, M. Vončina, B. Kosec, J. Medved, *Metalurgija.* **51**, 216–220 (2012)
27. W. Khalifa, F.H. Samuel, J.E. Gruzleski, *Metall. Mater. Trans. A.* **34**, 807–825 (2003). <https://doi.org/10.1007/s11661-003-1009-9>
28. T. Gao, K. Hu, L. Wang, B. Zhang, X. Liu, *Results Phys.* **7**, 1051–1054 (2017). <https://doi.org/10.1016/j.rinp.2017.02.040>
29. Y. Nemri, B. Gueddouar, M.E.A. Benamar, T. Sahraoui, N. Chiker, M. Hadji, *Int. J. Met.* **12**, 20–27 (2018). <https://doi.org/10.1007/s40962-017-0134-y>
30. M. Wang, *Control of morphology Al-Fe-Si phase in Al-Si-Cu hypoeutectic alloy*. Doctoral Thesis. Purdue University, West Lafayette, Indiana, (2014).
31. A. Fabrizi, G. Timelli, *The influence of cooling rate and Fe/Cr content on the evolution of Fe-rich compounds in a secondary Al-Si-Cu diecasting alloy*. *IOP Conf. Ser. Mater. Sci. Eng.* **117**, 012017 (2016). <https://doi.org/10.1088/1757-899X/117/1/012017>
32. S. Ferraro, A. Fabrizi, G. Timelli, *Mater. Chem. Phys.* **153**, 168–179 (2015). <https://doi.org/10.1016/j.matchemphys.2014.12.050>
33. C. Xu, F. Wang, H. Mudassar, C. Wang, S. Hanada, W. Xiao, C. Ma, *J. Mater. Eng. Perform.* **26**, 1605–1613 (2017). <https://doi.org/10.1007/s11665-017-2599-5>
34. H. Liao, Y. Sun, G. Sun, *Mater. Sci. Eng. A.* **335**, 62–66 (2002). [https://doi.org/10.1016/S0921-5093\(01\)01949-9](https://doi.org/10.1016/S0921-5093(01)01949-9)
35. K. Nogita, A. Dahle, *Scr. Mater.* **48**, 307–313 (2003). [https://doi.org/10.1016/S1359-6462\(02\)00381-0](https://doi.org/10.1016/S1359-6462(02)00381-0)
36. K. Nogita, A. Dahle, *Mater. Trans.* **42**, 393–396 (2001). <https://doi.org/10.2320/matertrans.42.393>
37. K. Nogita, A. Dahle, *Mater. Trans.* **42**, 207–214 (2001). <https://doi.org/10.2320/matertrans.42.207>
38. K. Nogita, A. Dahle, *Mater. Charact.* **46**, 305–310 (2001). [https://doi.org/10.1016/S1044-5803\(00\)00109-1](https://doi.org/10.1016/S1044-5803(00)00109-1)
39. F. Yılmaz, O.A. Atasoy, R. Elliott, *J. Cryst. Growth.* **118**, 377–384 (1992). [https://doi.org/10.1016/0022-0248\(92\)90086-X](https://doi.org/10.1016/0022-0248(92)90086-X)
40. A. Mazahery, M.O. Shabani, *JOM.* **66**, 726–738 (2014). <https://doi.org/10.1007/s11837-014-0968-1>
41. X. Liu, Y. Zhang, B. Beausir, F. Liu, C. Esling, F. Yu, X. Zhao, L. Zuo, *Acta Mater.* **97**, 338–347 (2015). <https://doi.org/10.1016/j.actamat.2015.06.041>

42. A.K. Dahle, K. Nogita, S.D. McDonald, C. Dinnis, L. Lu, *Mater. Sci. Eng. A.* **413–414**, 243–248 (2005). <https://doi.org/10.1016/j.msea.2005.09.055>
43. P. Srirangam, S. Chattopadhyay, A. Bhattacharya, S. Nag, J. Kaduk, S. Shankar, R. Banerjee, T. Shibata, *Acta Mater.* **65**, 185–193 (2014). <https://doi.org/10.1016/j.actamat.2013.10.060>
44. S.A. Hassasi, M. Abbasi, S.J. Hosseinipour, *Inter Metalcast.* **14**, 69–83 (2020). <https://doi.org/10.1007/s40962-019-00325-0>
45. M.M. Shehata, S. El-Hadad, M.E. Moussa et al., *Inter Metalcast.* **15**, 763–779 (2021). <https://doi.org/10.1007/s40962-020-00497-0>
46. Q. Li, J. Li, B. Li et al., *Inter Metalcast.* **12**, 554–564 (2018). <https://doi.org/10.1007/s40962-017-0193-0X>
47. A.P. Hekimoğlu, M. Çalış, *Trans. Nonferrous Met. Soc. China.* **31**, 2264–2276 (2021). [https://doi.org/10.1016/S1003-6326\(21\)65653-4](https://doi.org/10.1016/S1003-6326(21)65653-4)
48. X. Feaugas, H. Haddou, *Philos. Mag.* **87**, 989–1018 (2007). <https://doi.org/10.1080/14786430601019441>
49. G.K. Sigworth, R.J. Donahue, *Inter Metalcast.* **15**, 1031–1046 (2021). <https://doi.org/10.1007/s40962-020-00535-x>
50. G.K. Sigworth, *Inter Metalcast.* **2**, 19–40 (2008). <https://doi.org/10.1007/BF03355425>
51. M.S. Salleh, M.Z. Omar, J. Syarif, J. Alloys Compd. **621**, 121–130 (2015). <https://doi.org/10.1016/j.jallcom.2014.09.152>
52. Y. Alemdağ, M. Beder, *Mater. Des.* **63**, 159–167 (2014). <https://doi.org/10.1016/j.matdes.2014.06.006>
53. A.P. Hekimoğlu, G. Ayata, *Pamukkale Univ. J. Eng. Sci.* **25**, 49–55 (2019). <https://doi.org/10.5505/pajes.2018.46343>

**Publisher's Note** Springer Nature remains neutral with regard to jurisdictional claims in published maps and institutional affiliations.